

Universal Features of Non-equilibrium Ionic Currents through Perm-selective Membranes: Gating by Charged Nanoparticles/Macromolecules for Robust Biosensing Applications

Sebastian Sensale, Zeinab Ramshani, Satyajyoti Senapati, and Hsueh-Chia Chang*



Cite This: <https://dx.doi.org/10.1021/acs.jpcb.0c09916>



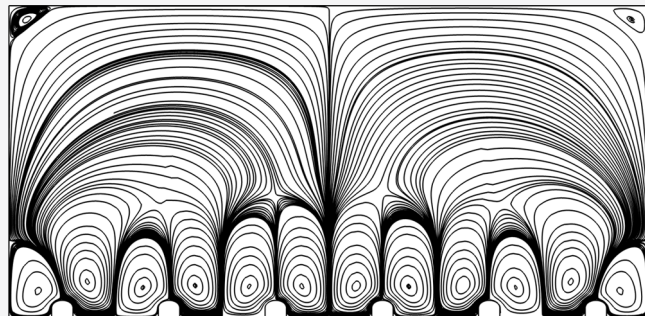
Read Online

ACCESS |

Metrics & More

Article Recommendations

ABSTRACT: The presence of a small number (~ 1000) of charged nanoparticles or macromolecules on the surface of an oppositely charged perm-selective membrane is shown to sensitively gate the ionic current through the membrane at a particular voltage, thus producing a voltage signal much larger than thermal noise. We show that, at sufficiently high voltages, surface vortices appear on the membrane surface and sustain an ion-depleted boundary layer that controls the diffusion length and ion current. An asymmetric vortex bifurcation occurs beyond a critical voltage to reduce the diffusion length and the differential resistance by half. Surface nanoparticles and molecules only affect this transition voltage in the membrane I – V curve. It is shown to shift by $2 \ln 10 (RT/F) \sim 0.12$ V for every decade increase in bulk target concentration, independent of sensor dimension and target/probe pair. Such universal features of the surface charge-sensitive nonlinear and nonequilibrium conductance allow us to develop very robust (a 2–3 decade dynamic range for highly heterogeneous samples with built-in control) yet sensitive (subpicomolar) and selective biosensors for highly charged molecules like nucleic acids and endotoxins—and for proteins with charged nanoparticle reporters.



INTRODUCTION

Ion-selective nanoporous polymer membranes of both charges have been used commercially for 6 decades and their nonequilibrium electrokinetic phenomena have been scrutinized for an equally long period. Recently, several new analyte concentration and molecular detection technologies based on the same ion-selective membranes have been reported for microfluidic analyte manipulation and biosensing (see, for examples, reviews by Berzina and Anand¹ and Slouka et al.²). Nonequilibrium ion current through the perm-selective membrane is highly nonlinear with two distinct jumps in the differential resistance at V_{lim} and V_o that demarcate the I – V curve into three distinct underlimiting (UR), limiting (LR), and overlimiting regions (OR) as the voltage increases³ (see Figure 1). These three regions exist for all perm-selective membranes. The transitions occur due to ion depletion and then convective remixing by a microvortex instability on one side of the membrane. (The membrane conductance is typically so high that its resistance can be neglected.) These nonequilibrium and asymmetric concentration, charge, and hydrodynamic polarization phenomena across a perm-selective membrane endow its I – V curve with reproducible universal features, particularly in the OR region, that will be explored here for the purpose of charge-based molecular sensing. That

the microvortices are driven by a Debye-length dimension extended (charge) polarized layer (EPL)³ suggests that the ion current in the OR region can be very sensitively gated by charged macromolecules on the membrane surface. Membrane sensors hence become low-cost electrokinetic analogs of field-effect transistor sensors. In fact, since the depletion action controls the local ionic strength and the voltage controlled by the macroscopic ion-depleted region is in excess of 0.1 V, these membrane sensors are very robust—they are not sensitive to bulk ionic strength variations that affect Debye screening (as the depletion action controls the local ionic strength at the membrane), to the identity of the target/probe pair and, with the proper voltage signal selection, to the sensor geometry or membrane selection. Its large voltage signals, much larger than thermal noise, also produce better detection limit than electrochemical sensors. As the membrane is charged and its surface is highly hydrophilic, there is very little nonspecific

Received: November 5, 2020

Revised: December 14, 2020

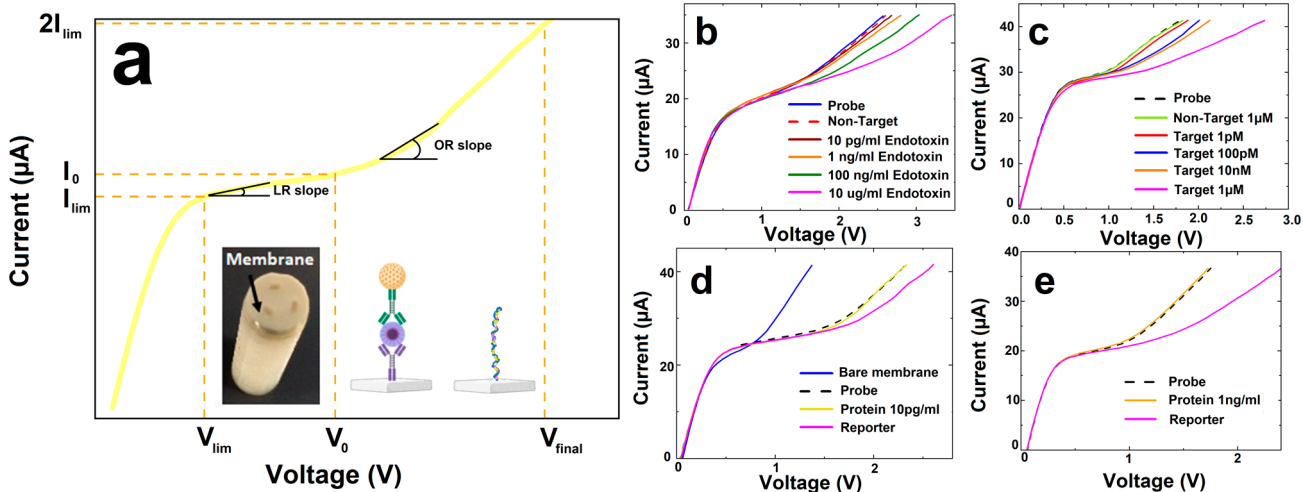


Figure 1. (a) Schematic of a typical I – V curve of an ion-exchange membrane sensor. The transition voltages V_{lim} and V_0 (and their respective currents) that demarcate the UR, LR and OR regions are indicated. The scan terminates at roughly $2I_{lim}$. The voltage shift at $2I_0$ current is often taken as the voltage signal, as the curves only change in the OR region. The relevant slopes that represent the inverse differential resistance estimated in the theory are also indicated. (Insets) (Left) Typical 3-membrane sensor capillary module with electrodes inserted into 3 compartments in the capillary. (Right) Schematics of the nucleic acid probe-target and antigen probe-target-reporter complexes on the membrane surface. (b–e) I – V curve after probe functionalization and target hybridization at different bulk concentrations for endotoxin (b), nucleic acid (c), and proteins Angiogenin (d) and Endothelin (e). For nucleic acids and endotoxin, I – V curves with nontarget molecules are also inserted. For proteins, significant shift is only achieved with a nanoparticle reporter attached to a reporter antibody. All the probes, targets, reporters, and nontargets are specified in the Materials and Methods. The scan rate is $1 \mu\text{A}/\text{s}$ and the I – V curves have been shown to be independent of scan rate at this value.

adsorption and hence blocking agents are unnecessary. Finally, the shear produced by the microvortex also minimizes nonspecific binding, although a controlled wash is often still necessary.

Unlike electrochemical sensors based on conductance (cyclic voltammetry) or impedance, the I – V curves of the membrane sensors are remarkably similar, with the target molecules contributing only to one feature—the onset of the OR region. The invariance in the other lower voltage regimes allows a built-in control to ensure the efficacy of the membrane sensor, much like the control strip of a lateral flow assay. However, there has been no theory on the voltage signal corresponding to the shift in the onset voltage of the OR region. Availability of such a theory would enable the development of robust standard calibration curves and the design of new sensors for different probe-target pairs. We report such a theory in this paper. We shall present the theory for an anion-selective (positively charged membrane) with negatively charged nucleic acid targets and silica nanoparticle reporters. However, the theory is equally applicable to cation-selective membranes with positively charged targets or reporters, once the bias voltage is reversed.

The transition at $V_{lim} \sim (RT/F)$ (25.6 mV) to a limiting current due to ion depletion on one side of the membrane has been known for over 70 years.⁴ For an ideally selective membrane with zero co-ion flux, the co-ion electromigration flux and diffusive flux cancel each other on the ion depletion side of the membrane. The co-ion is hence at quasi-Boltzmann equilibrium and its concentration $c_0 \exp(-\phi z F/RT)$ is much lower than its bulk ion concentration c_0 by a Boltzmann factor that is exponentially dependent on the local potential ϕ . This implies that, for a symmetric and electroneutral binary electrolyte whose co-ion and counterion concentrations are equal, the electromigration and diffusive fluxes of the counterion are equal and in the same direction, resulting in a

purely diffusive description for the counterion with twice the natural diffusivity D .⁵ Electroneutrality stipulates that, for a symmetric electrolyte, the co-ion concentration is equal to this diffusion-controlled counterion concentration at every position. Due to the conductivity jump at the membrane surface, counterions are depleted on one side of the membrane and its surface concentration decreases with increasing voltage, thus creating an ionic strength gradient that is responsible for the nonequilibrium phenomena. Even at the lowest voltages in the UR, ion depletion can occur such that the electrolyte ionic strength deviates from the homogeneous limit when the ion flux is purely due to equilibrium electromigration with a counterion-carried ion current flux density $2(Dz^2/RT)c_0 V/L'$, where L' is the electrode separation.

The UR differential resistivity (resistance times area divided by L') is then $(RT/2c_0 Dz F^2)$, the slope of the linear I – V curve in the UR. The first transition at V_{lim} occurs when the counterion concentration vanishes on the membrane surface and diffusion begins to contribute to the ion current. Since counterion flux under this inhomogeneous condition is still described by the diffusion equation, just with twice the diffusivity, a limiting counterion flux density of $j = 2Dc_0/L$ is obtained. It carries a current density of $i_{lim} = 2DzFc_0/L$, where L is the thickness of the diffusion layer. This diffusion length can be the thickness of a convective boundary layer established by tangential or stagnation flow, which can be sized in micrometers. It could also be the distance to the electrode in a quiescent pseudo-one-dimensional geometry, which can be as large as a few centimeters. For small membranes with dimensions much smaller than any macroscopic length scale, it could also be the radius or some characteristic width of the membrane. Since this limiting current density is independent of voltage, it represents an infinite resistivity compared to the finite value in the UR.

Rubinstein and Shtilman⁶ first noted that in the LR beyond V_{lim} , if the co-ion retains the quasi-Boltzmann concentration $c_0 \exp(-z\phi F/RT)$ dependence on the local potential ϕ , a vanishing concentration at the membrane surface would mean an infinitely large voltage drop V . To remove this singularity, they introduced a charged extended polarized layer (EPL) at the membrane surface, with the same charge as the counterion and roughly the dimension of the Debye layer, to smooth out this singularity. The EPL separates the electro-neutral region of the diffusion layer from the membrane so that the co-ion concentration in the electro-neutral region never vanishes and can still obey Boltzmann equilibrium. Ben and Chang⁷ showed theoretically that, for small L , this EPL can reduce the diffusion length and hence produce a finite differential resistance in the LR, instead of the infinite one predicted by Levich's theory. With matched asymptotics, Ben and Chang⁷ also showed that the $I-V$ curve in the LR is linear with a differential resistance very different from the UR regime, whose current density can be described by (see Ben and Chang⁷)

$$i - i_{lim} = -Fj = \frac{2zF^2 D c_0}{LRT} \left(\frac{3\lambda_D}{2L} \right) (V - V_{lim}) \quad (1)$$

for most realistic conditions, where λ_D is the Debye length. They were able to collapse their LR numerical data, and Yossifon et al. were able to collapse their LR experimental data from ion-selective nanoslots.⁸ The LR resistivity based on the electrode separation L' is hence higher than that in the UR by a factor of $\left(\frac{2L}{3\lambda_D}\right)\left(\frac{L'}{L}\right)$. Hence, it becomes finite if the electrode separation L' is much larger than the diffusion length L . Such conditions are usually satisfied with small membrane biosensors with a small L , such that the $I-V$ curve in the LR has a finite slope and resistivity (see Figure 1).

The transition to OR at V_o , which is an increment of several RT/zF beyond V_{lim} , has been explored numerically (see recent review by Mani and Wang⁹) but a clear scaling theory like (1) for the OR has not yet been developed. Yossifon et al.⁸ have shown that it has roughly the scaling as (1) but by a different diffusion length, which they fitted empirically, which can be less than $L/2$, giving rise to an OR $I-V$ slope that is more than twice that in the LR (more than $1/2$ in differential resistance). The physical mechanism for this jump in differential resistance at V_o is quite clear from numerical simulations. An electro-osmotic instability of the EPL produces microvortices that reduce the dimension L of the ion depletion region in the LR. This instability was first predicted by Rubinstein and Zaltzman¹⁰ and was first independently observed by Rubinstein et al.¹¹ and Yossifon and Chang¹² simultaneously. What exactly is the reduced diffusion length due to the microvortex instability remains unknown. In the transient experiments of Yossifon and Chang, the vortices seem to coalesce and grow in size until they reach a critical value at each given voltage. Beyond a certain voltage, they grow to sufficient size to trigger the transition to OR. Such prior knowledge on the nonequilibrium electrokinetic phenomena of ion-transport through perm-selective membranes will be integrated here to examine the sensitivity, selectivity, and robustness of membrane sensors of biomolecules.

MATERIALS AND METHODS

Materials. Phosphate buffered saline (PBS) and $10 \times$ TAE buffer consisting of 400 mM Tris-acetate and 10 mM ethylenediaminetetraacetic acid (EDTA) were purchased from Fischer Scientific and used as received. Silicon RTV system and Quick cast polyurethane resin were purchased from TAP Plastic Inc. (San Leandro, CA). 1-Ethyl-3-(3-(dimethylamino)propyl)carbodiimide (EDC), benzophenone-3,3',4,4'-tetracarboxylic acid, and sodium hydroxide were purchased from Sigma-Aldrich (St. Louis, MO). The target miR-21 (TAGCTTATCAGACTGATGTTGA) is a common cancer biomarker. Their model sequences and complementary oligo probes were purchased from Integrated DNA Technologies. The Angiogenin (ANG), Endothelin-1 (ET-1), and Placental Growth Factor (PlGF) antigens were 265-AN-050/CF from R&D, aa 1-212 from Abcam and 364-PGB-010/CF from R&D. Their capture/reporter antibodies were Human Angiogenin Antibody/ab241874 from Abcam, ab117757 from Abcam/H00001906-M01 from Novus Biologicals, and Human PLGF Antibody/ab267683 from Abcam.

Fabrication of Ion Exchange Membrane Sensor. An anion-exchange nanoporous membrane was used as a sensor. The membrane is composed of polystyrene–divinylbenzene fine particles with strong basic quaternary ammonium groups supported by polyethylene as a binder and polyamide/polyester textile fiber (Mega a.s., Czech Republic). To fabricate a sensor, a small piece of hand cut membrane was embedded in the sensor capillary module shown in the insets of Figure 1 using a polyurethane resin. The membrane was placed on top of a silicone mold with poles. A microscope glass slide containing a PDMS layer was used to sandwich the membrane. A two-component polyurethane resin (1:1 ratio) was transferred inside the mold and allowed to cure for 30 min. A detailed fabrication process can be found in our previous reports.^{13,14} The fabricated sensor module of Figure 1 was then functionalized with a probe complementary to target miRNA, ssDNA, or target antigen using EDC coupling chemistry. Prior to functionalization the –COOH groups were attached to the membrane surface using UV treatment as discussed earlier.¹³

Fabrication of Microfluidic Device. The microfluidic devices were made from three layers of polycarbonate sheet of 0.3 mm thickness using thermal/pressure bonding technique.^{13,14} The middle layer had a cut out of microfluidic channel whereas the top layer had the cut outs of orifices for the inlet, outlet, sensing and concentration units. The fabricated biochip contained a sensor chamber to mount a one or multiple membrane sensor module, separate reservoirs to place source and reference electrodes for current–voltage measurement, and inlet and outlet for sample and buffer injection. For miRNA detection, the concentration unit was also added to the device by two orthogonally placed reservoir which were connected to the main microfluidic channel via cation exchange membrane.

Recording Unit. To obtain the current–voltage characteristics, a Gamry 500 potentiometer (Gamry Instrument) connected to a PC was used, where an electric current was applied through the membrane sensor the upstream via two platinum electrodes and the voltage drop across the membrane sensor was measured by two reference electrodes (Ag–AgCl).

Experimental Method. In a typical experiment, functionalized sensor was mounted in the device and the CVC (Current-Voltage-Characteristic) measurement was performed

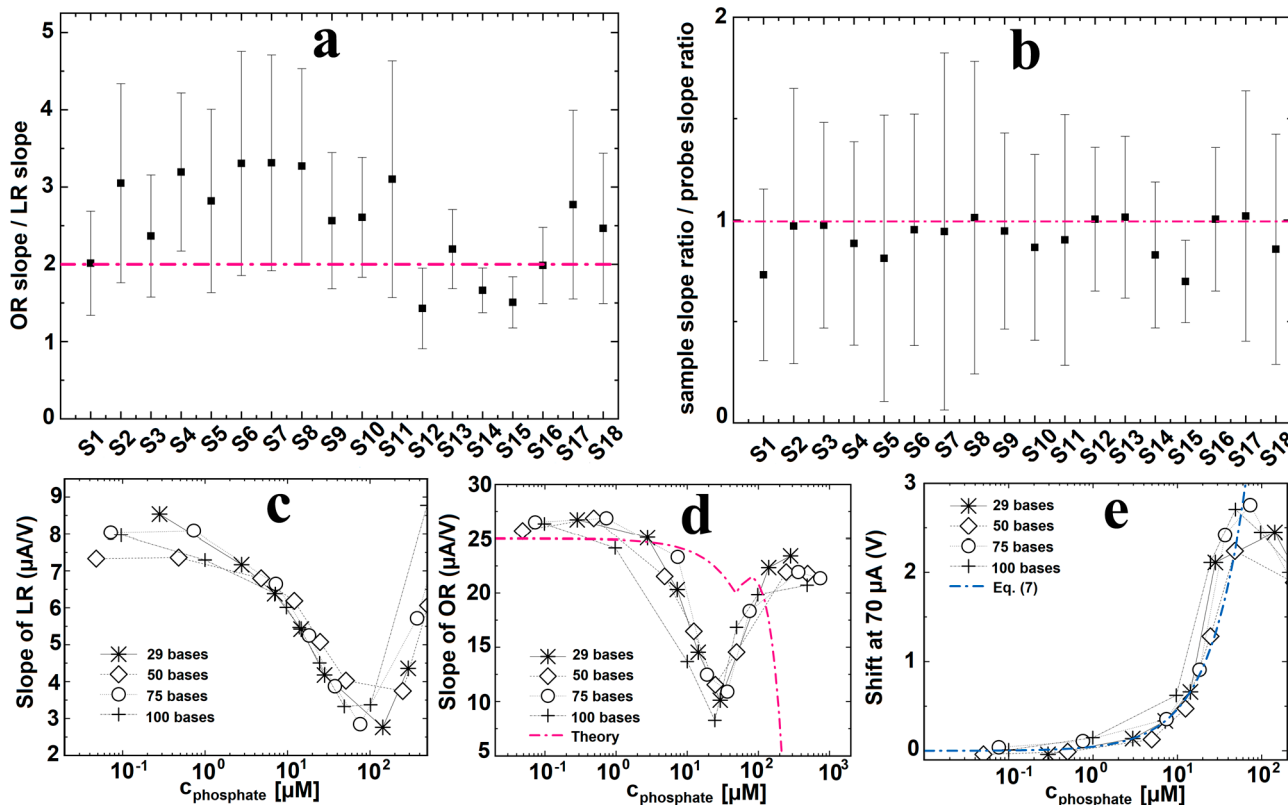


Figure 2. (a and b). Invariance in the slope ratios of the OR and LR curves (with variations along the curves represented by the error bars) of 18 different sensors for a protein–target–reporter complex for Placentia Growth Factor (Sensor 1), Endothelin-1 (Sensors 2–10) and Angiogenin (Sensors 11–18). Typical I – V curves for the latter two are shown in parts d and e of Figure 1, with very different dynamic ranges (see Figure 3). (a) The ratio of OR slope to LR slope was measured after introducing the target protein and reporter. (b) The ratio of OR slope to LR slope was measured, before and after protein target/reporter hybridization. (c and d) Slopes of the LR and OR regimes as a function of nucleic acid target concentration for targets with different bases. (e) Shift at $I = 70 \mu\text{A}$, which is about $2I_o$ before hybridization. This shift is close to the shift in V_o . Due to the uncertainty in $V_o(C)$ after hybridization, this alternate shift is chosen. The theoretical curves in parts d and e are from (6) and (7), respectively, with bulk ionic strength $c_0 = 16 \text{ mM}$, a fitted target concentration with minimum OR slope $C_{\min} = 40 \mu\text{M}$, and a diffusion length $L = 2.5 \mu\text{m}$.

with $0.1 \times$ PBS in the microchannel and used as the baseline. Raw samples from cell culture media or plasma are inserted into the chip.^{13,14} After target hybridization another CVC measurement was conducted and compared to the baseline to measure the voltage shift, which was in direct contact with target concentration in the sample. Before CVC measurement the non specifically adsorbed analytes were removed from the membrane surface using PBS washes. The detection experiment was performed by 20 min incubation of the samples for hybridization of the target with the probes attached to the sensor surface. A membrane-based concentration technique was used to concentrate the target beneath the sensor by applying the electrical field to enhance the sensitivity and the limit of the detection. In case of protein detection, a silica reporter was made by conjugation of the detection antibody with 50 nm silica particle and incubated in the microchannel after target protein hybridization. The use of silica reporters enhances the CVC signal, since proteins are inherently poorly charged and insufficient to cause any voltage shift.

RESULTS AND DISCUSSION

It is reasonable to assume that the reduced diffusion length is sensitive to the charge in the EPL, as the instability is caused by the EPL. This suggests a few charged molecules and nanoparticles within $\sim 10 \text{ nm}$ EPL (no more than 10× the

Debye length) can shift V_o by values on the order of RT/zF or larger. This has been the basis of a membrane sensor technology in our lab.^{13–19} The molecules can adsorb onto the small membrane sensors of dimension $100 \mu\text{m}$ or, to detect specific molecules, we functionalize specific oligo or antibody probes onto the membrane that can hybridize with the target. The membranes are then inserted into electrode capillaries which can, in turn, be inserted into a sample reservoir with counter electrodes (see Figure 1a). In parts b and c of Figures 1, we show typical I – V curves for highly charged nucleic acids and endotoxins. Specific sensor I – V curves after probe functionalization and after hybridization in a particular target concentration are shown. A clear change in the I – V curve is observed after hybridization. If the target molecules (mostly proteins) are uncharged or weakly charged, we introduce a reporter antibody with a 50-nm-diameter (highly charged) silica nanoparticle as charged reporter, as seen in parts d and e of Figures 1. The I – V curve does not change after target introduction, but a large change is observed after the nanoparticle reporters are added. These nanoparticle reporters offer an additional advantage: selectivity. Since they are larger than the protein target, nonspecific bound nanoparticles can be sheared off more readily during the wash step to remove nonspecifically bound reporters.

The protein samples in Figure 1 are raw cell culture media and the nucleic acid samples are heterogeneous plasma samples.¹⁴ Despite the heterogeneous nature of the sample, the varying target size and charge, and the different sensor size (hundreds of micrometers to 10 mm in radius), all the *I*–*V* curves show the signature transitions from UR, LR and OR, as indicated by the schematic in Figure 1a. It is also obvious that the OR region is most sensitive to the concentration of the target molecule, with a voltage shift to the right with increasing target concentration but without significant change in the slope (differential resistance). The *I*–*V* curves for all sensors and with different target concentrations are hence remarkably self-similar, suggesting they can be collapsed with proper normalization. This invariance is confirmed in Figure 2a, where the ratio of the differential resistance (slope of the *I*–*V* curve at the onset) in the OR and LR regions are shown to be close to 2 for 18 different protein sensors and three different targets with different capture/reporter antibodies. For all these 18 sensors, the slopes of the LR is shown to be nearly identical before and after target/reporter hybridization. The key signal is then the shift in the transition voltage V_o from LR to OR, with the rest of the IV curve insensitive to the presence of the target molecules on the membrane surface. Different sensor areas will produce different currents I but nearly identical voltage signals in V_o . At the subpicometer range of Angiogenin (Figures 1d and 3), we estimate fewer than 1000 nanoparticles on the smallest (500 μm) membrane.

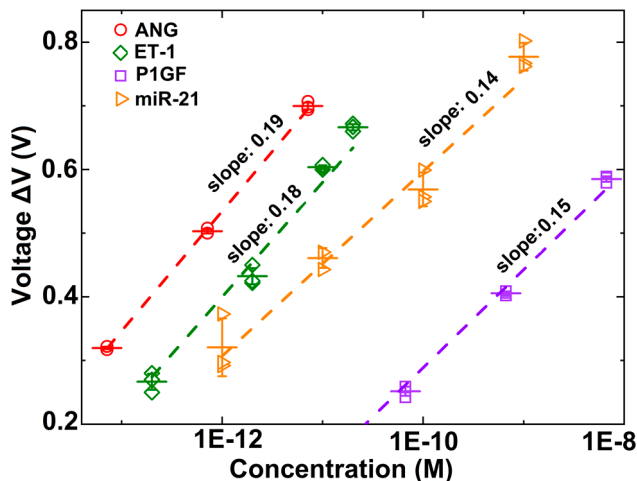


Figure 3. Voltage shift in the OR region for a nucleic acid (microRNA) target (miR-21), protein targets with 50 nm nanoparticle reporter (Endothelin-1 (ET-1), Angiogenin (ANG), and Placental Growth Factor (P1GF)) at different target concentrations.

A closer scrutiny shows even more universality in Figure 2c–e. We were able to collapse both the LR and OR slopes for nucleic acid targets by using the charge concentration instead of the molecular concentration. The collapse shows it is the charge concentration that is behind the universality. We note that both slopes exhibit a minimum with respect to the target charge concentration.

To remove any sensitivity to membrane area, which is difficult to control, we focus on the voltage shifts ΔV of the transition voltage to OR, $V_o(C)$, due to the presence of molecules of bulk target molecule concentration C that has adsorbed or hybridized (with specific probes) onto the membrane. From Figures 1 and 2, this seems to be the only

feature in the *I*–*V* curves that is sensitive to the presence of surface target molecules. A shift ΔV of several RT/F is observed and the limit of detection is often fewer than 1 million molecules in the bulk or as low as 1000 on the surface. As evident in Figure 3, all calibration of voltage shift vs C , shows a logarithm dependence on the bulk concentration C at low concentrations. This near universal slope is roughly between 4 to 8 RT/F (0.1 to 0.2 V) per decade change in C . It is independent of whether the charged nanoparticles are RNAs or silica nanoparticles. The up and down shift is due to affinity of the bulk molecule to the surface probe, but the slope is always the same. This universal log C behavior breaks down at higher concentration, as seen in Figure 2e for DNAs of different lengths.¹⁷ Instead, a linear C scaling is observed for one decade in the high C region bounded by the curious minimum in the slope at a critical C (a maximum in the differential resistance) of the overlimiting *I*–*V* curve. At low concentrations, the same logarithmic dependence of Figure 3 is recovered. At all concentrations for three different protein targets and a nucleic acid target, the slope S_o of the *I*–*V* curve in the OR region is roughly 1.5 to 2.5 times the slope S_L in the LR (see Figure 2, parts a, c, and d), even though the OR *I*–*V* curve is clearly shifted to the right with higher concentrations. This curious universality is even obeyed when both slopes exhibit a minimum at high DNA concentrations.

We offer a theory for such remarkable universality in the slopes and for how the voltage shift in the OR regime, as measured by $V_o(C)$, depends on concentration. Transition from LR to OR on membrane surfaces with step-like patterns has been studied numerically and experimentally by De Valen  a et al.²⁰ They found unpatterned membranes to produce moving and chaotic vortices whereas patterned membranes have vortices pinned to the corners of the steps. Although the initial vortex spacing seems to be exactly the structure spacing, they grow and sometimes merge to form a mixing layer of universal dimension L_{mix} between 350 and 500 μm , independent of the structure spacing or even without patterns. The ion concentration gradient is mostly in this mixing layer, and hence L_{mix} becomes the reduced diffusion length L in the OR. These vortices are mostly due to field penetration across the membrane step and are hence similar to what is known as Dukhin vortices.³ Similar Dukhin vortices were also seen in the numerical simulations and experimental studies of Davidson et al.,²¹ where they are pinned to the junction between permeable and impermeable portion of the membrane surface. They also observe roughly a factor of 2 reduction in finite resistance in the OR because of the steps, as we have seen in Figure 2 for charged molecules and reporters. Although a near universal reduction of 2 in resistance is observed with the two patterns, neither studies observe a shift in the OR *I*–*V* curve (corresponding to an increase in resistance) due to the presence of their structures, as we have observed for charged molecules or nanoparticles in Figure 1. This suggests that the shift we observed is due to vortex dynamics unique to our charged targets and nanoparticle reporters. They do not exist for pinned vortices or vortices on patterned surfaces. We will show that specific vortex pattern bifurcation that leads to a shift in the OR curve is only possible with point charges. There is hence something unique in the voltage shift due to the presence of charged molecules and nanoparticles that is independent of the universality of the slope ratio. Nevertheless, these prior works suggest that a steady-state solution exists on systems with patterned surfaces,

simplifying the numerical effort. Recent imaging studies by Bellon et al.²² and numerical efforts²³ showed that small ($\sim 600 \mu\text{m}$) and curved membranes produce very stable vortices that do not migrate as on larger flat membranes. Pinning by edges in a small domain should hence produce robust and steady vortices with reproducible OR I - V curves and, we suspect, so do charged molecules and particles.

The existence of steady-state vortices significantly reduces the computational effort. We conducted steady-state continuum simulations of the Poisson–Nernst–Planck and Navier–Stokes equations for a symmetric, binary, single-valent electrolyte with equal diffusivity of cations and anions $D = 2 \times 10^{-9} \text{ m}^2/\text{s}$, water dynamic viscosity $\mu = 0.001 \text{ Pa}\cdot\text{s}$, and permittivity $\epsilon = 80\epsilon_0$ (with ϵ_0 the vacuum permittivity). The domain is of width w and height L between an anion-selective membrane at zero potential and an electrode with a voltage of $V_0 < 0$. The side walls are field/flow/flux insulated and do not allow hydrodynamic slip. We model the charged particles or molecules on the membrane as localized structures with height h , width d and with a circular tip of diameter d . A fixed surface charge $\sigma < 0$ is assigned to each of these particles. There are n such particles and hence their spacing is w/n , with the first and last particles placed at a distance of $w/2n$ from the side walls. No-slip, a fixed anion concentration $2c_0$, and no-flux condition for cations are imposed on the membrane to make it be anion-selective. On the electrode, no slip and bulk anion and cation concentrations $c_0 = 1 \text{ mM}$ are imposed. Exhaustive COMSOL meshing analysis, with refined meshes of about 1 000 000 elements, were used to solve the full PNP-NS system. Rigorous convergence studies were carried out for each chosen set of parameters.

From our steady-state simulations, we were able to reproduce the discontinuous jumps in differential resistance and observe three distinct UR, LR, and OR regimes for all the parameters we simulated except for very close nanoparticle separation (see Figure 4). Their slopes and shifts with increasing particle density are quite similar to those measured in Figure 1. The charged particles have stabilized the vortices to produce robust and reproducible quasi-steady I - V curves, including in the OR region (see Figure 5). The vortices appear very early in the LR (see Figure 6). The primary LR vortices

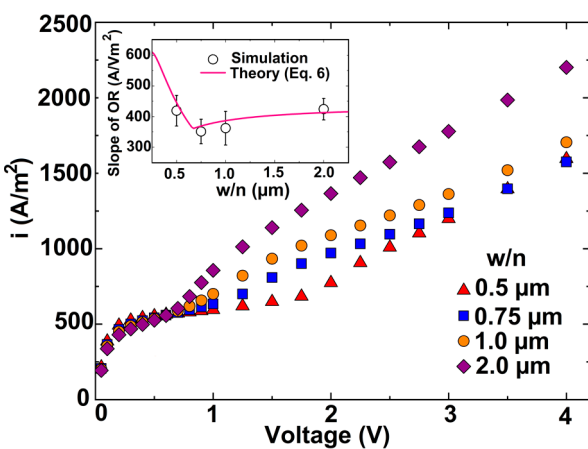


Figure 4. Simulated I - V curves for $L = 1 \mu\text{m}$, $d = 100 \mu\text{m}$, $\sigma = -0.035 \text{ C}/\text{m}^2$ and w/n from 0.5 to 1 μm . (Inset) Numerical (symbol) and theoretical (line, eq 6) estimates of the slope of the OR under the same conditions. A shallow minimum in the slope with respect to the particle concentration is quantitatively captured by our theory.

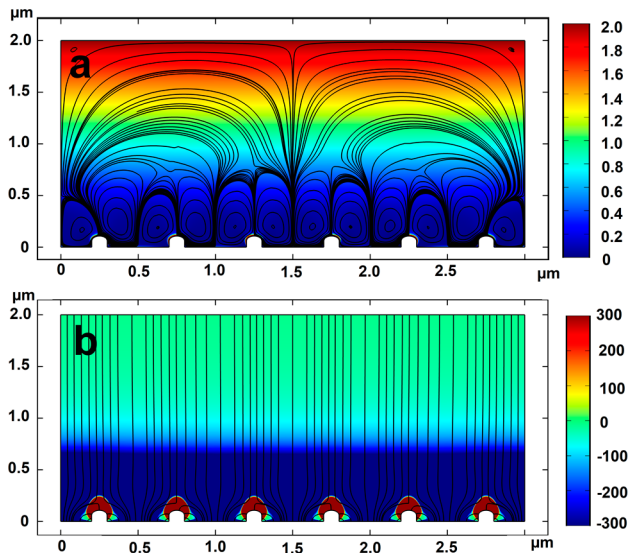


Figure 5. Fluid flow streamlines and (color, in mM) ionic strength (a), electric field lines and (color, in C/m^3) space charge density (b) for $L = 2 \mu\text{m}$, $V = 1 \text{ V}$, $\sigma = -0.035 \text{ C}/\text{m}^2$, and $w/n = 0.5 \mu\text{m}$.

are sandwiched between the charged nanoparticles, with one vortex pair between two adjacent particles. Vortex pairs exhibit high mirror symmetry about the nanoparticle. Each vortex of the pair is, however, elliptic, with a height roughly $3/2$ the spacing and the width $1/2$ the nanoparticle spacing. The center of each vortex is also shifted toward the nanoparticle. This suggests that the maximum electric force is between the vortex center and the nanoparticle. This is confirmed in Figure 5b, where an intense space charge density and electric field is observed between the nanoparticle and the oppositely charged membrane. This highly charged region occupies a width $d + 2\lambda_0$ at each nanoparticle, where $\lambda_0 \sim 100 \text{ nm}$ is the local Debye length in the ion depleted region. These strong charge monopoles then produce very high electroosmotic velocities, in excess of $u = 1000 \mu\text{m}/\text{s}$ (at 0.1 V, 10 000 at 1 V), that drive the vortices. As a result, despite the small scale of the primary vortices, they maintain the low ionic strength within the vortices and essentially reduce the diffusion length from L to the height of the vortices, such that $L_{\text{mix}} = 3w/2n$ becomes the effective diffusion length. Our estimate of the lowest Peclet number UL_{mix}/D is about 0.5 at 0.1 V (and 5 at 1 V), confirming the mixing effect of the primary vortices. (See, for example, Roberts and Chang²⁴ on how high Peclet number vortices can homogenize the concentration field within the vortex. In this case, it extends the ion depleted region near the membrane surface that controls the ion flux—the blue region in Figure 5.) For large particle spacing, L_{mix} exceeds L and the diffusion length retains the original value L of the domain height.

The vortex pair with mirror symmetry between the nanoparticles grows in amplitude as the voltage increases in the LR. One of the vortices of each pair begins to dominate away from the membrane surface, such that a symmetric vortex pair with mirror symmetry becomes an asymmetric one with the smaller vortex about half the size of the original vortices. This symmetry-breaking vortex bifurcation occurs for all nanoparticle spacings. The transition V_o occurs roughly when the symmetry-breaking vortex bifurcation occurs, as seen in Figure 6. The diffusion length now reduces by a factor of 2 as the smaller and faster vortices dominate the depletion action

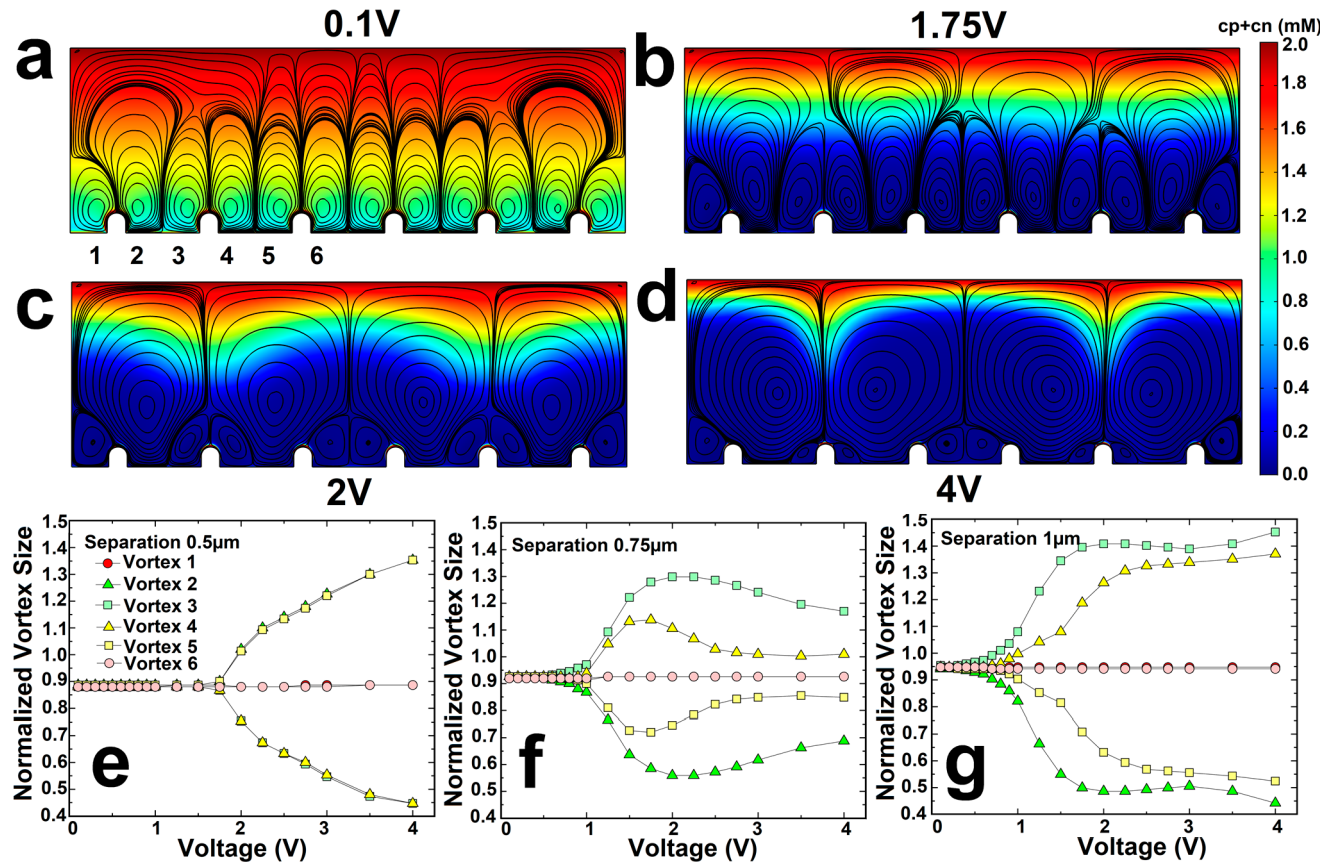


Figure 6. Asymmetric bifurcation of the microvortices and transition to OR. (a–d) Vortices in the ohmic region (0.1 V), near the transition to the overlimiting region (1.75 and 2 V), and on the overlimiting region (4 V) for $w/n = 0.5 \mu\text{m}$, $\sigma = -0.035 \text{ C/m}^2$, and $L = 1 \mu\text{m}$. Small numbers are the vortex numeration for parts e–g. Initially, the center of the vortices is found near the particles, and they move away from them toward the middle between particles as we increase the voltage. They then compete to occupy the full spacing, where the overlimiting current starts, when every other one becomes larger and the others smaller. The smaller one is about half the size of the original vortex before the asymmetry bifurcation. (e–g) Horizontal vortex size near the anion-selective membrane as a function of the imposed voltage for different values of w/n . Vortex numeration goes from left to right. Only the left half of the simulation box is considered, and vortex sizes are normalized by half the separation between nanoparticles.

near the membrane. (Compare the ionic strength contours at 0.1 and 2 V in Figure 6 and note the diffusion length $3w/2n$ of the primary vortices, with high ionic strength gradient, at 0.1 V is reduced by half at 2 V when its bottom half defined by the blue contours is removed by the depletion action of the smaller secondary vortices). This then explains the roughly factor of 2 increase in the slope of the I – V curve at V_o in the data of Figure 2a. The asymmetric vortex bifurcation to form small vortices half the size near the nanoparticles is responsible for this reduction in diffusion length. The differential resistance drops by a universal factor of 2. As the spacing w/n increases, the diffusion length eventually saturates at the domain height L . This transition is also reflected in the OR slope and is evident in the experimental data of Figure 2d, where the slope exhibits a minimum with respect to w/n . We will quantify this phenomenon and other phenomena with a scaling theory.

We begin by correcting (1) for the presence of the nanoparticles. Adjusting for the membrane surface excluded from ion flux by the nanoparticles and recognizing that the diffusion length is reduced, we obtain a scaling for the linear IV curve in the LR,

$$i - i_{\lim} = -Fj = \frac{2zF^2Dc_0}{LRT} \left(\frac{3\lambda_D\chi}{2L_{\text{mix}}} \right) (V - V_{\lim}) \quad (2)$$

where $\chi = \left(1 - \frac{n}{w}(d + 2\lambda_0) \right)$ and L_{mix} is the smaller of the diffusion length L and $3w/2n$, representing the new diffusion length in LR. The transition to OR at V_O occurs along this curve. For the OR region, we revise the LR formula with one that is twice the slope and with a different intercept at V_O

$$i - i_o = -Fj = \frac{2zF^2Dc_0}{LRT} \left(\frac{3\lambda_D\chi}{L_{\text{mix}}} \right) (V - V_o) \quad (3)$$

The key issue is then how V_O changes with particle density w/n , which now represents the concentration of charged target molecules on the membrane surface. The relevant velocity is the electroosmotic velocity at the nanoparticle that is driving the vortex bifurcation seen in Figure 6. In the highly depleted region with large λ_0 , its ζ potential scales as a logarithm function of the surface charge density (see subsequent discussion or Chang and Yeo⁵). Hence, the electroosmotic velocity u scales linearly with the voltage V , with a weak dependence on particle size or charge. This electroosmotic flow with a wall shear rate of $\mu u/\lambda_0$ needs to drive a vortex of width $w/2n$ near the surface. Hence, the total force (per unit transverse direction) needed to drive a vortex of width $w/2n$ (total viscous force) is the product of the velocity with the

vortex width, which scales as $Vw/2n$. Hence, V_o should scale as $2n/w$. We designate

$$V_o = \left(\frac{2nl}{w} \right) \left(\frac{RT}{zF} \right) \quad (4)$$

where l is a natural length scale corresponding to the vortex size at the OR transition without the nanoparticles. We hence obtain from (2),

$$i_o = i_{\text{lim}} + \frac{2zF^2Dc_0}{LRT} \left(\frac{3\lambda_D\chi}{2L_{\text{mix}}} \right) (V_o - V_{\text{lim}}) \quad (5)$$

With the diffusion length L being the distance from the membrane to the electrode in this planar simulation and $L_{\text{mix}} = \min\left\{L, \frac{3w}{2n}\right\}$, there is hence only one empirical parameter l for the size of the natural vortices at onset. We were able to collapse all the simulated LR and OR data, with widely ranging charge particle spacing, density and diffusion length, by (2) and (3) in Figure 7 with a selected length scale

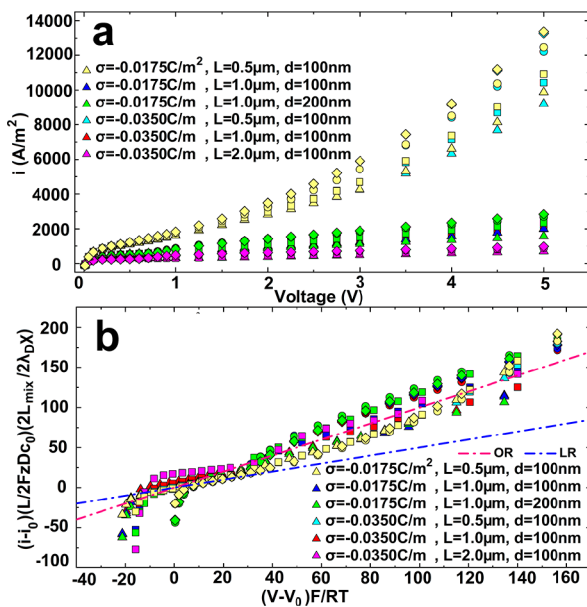


Figure 7. (a) Simulated I – V curves. Multiple values of w/n (triangle = 0.5 μm , square = 0.75 μm , circle = 1 μm , and diamond = 2 μm) were considered, as well as a range of σ , L , and d were considered (see image legend). (b) Collapse of simulated I – V curves in the OR region by eq 6 (red line, normalized). The LR data (blue line) also collapse but with one-half the slope. Due to the shift to V_o , the LR tail at low voltage does not collapse. The red theoretical curve is (5) with $l = 8 \mu\text{m}$. The blue theoretical curve is (5) with $1/2$ the slope.

of $l = 8 \mu\text{m}$. This parameter may represent the size of the natural vortices if there are no particles present. This dimension of natural vortices is consistent with that observed by Yossifon and Chang¹² for a nanoslot and by Bellon et al.²² for a 300 μm membrane. That the OR I – V slope is twice that of the LR is clearly evident in the collapsed plot of Figure 7, where the theoretical slopes do not involve the lone fitted parameter l .

The slope of the overlimiting I – V curve (in ohms per area) can be obtained explicitly, without adjustable parameter, as

$$\begin{aligned} S_0 &= \frac{2zF^2Dc_0}{LRT} \left(\frac{3\lambda_D\chi}{L_{\text{mix}}} \right) \\ &= \frac{2zFDc_0}{L} \frac{3\lambda_D \left(1 - \frac{n}{w}(d + 2\lambda_0) \right)}{\min\left\{L, \frac{3w}{2n}\right\}} \end{aligned} \quad (6)$$

The min bracket is there because the vortex size cannot be larger than the electrode separation. For small spacing w/n , this slope decreases with increasing particle spacing w/n as $1/(w/n)$ and for large spacing, it increases with w/n until $w/n = 2(d + 2\lambda_D)$. Thus, a minimum occurs at roughly $3w/2n = L$, when the vortex size exceeds the diffusion length. Below it, the vortex size controls the diffusion length and the ion flux. Above it, the vortex size saturates at L , and the reduction in membrane blockage begins to dominate with increasing w/n . These trends are also quantitatively confirmed in the simulated I – V curves of Figure 4 (see inset), where the measured slope is compared to (6) without adjustable parameters. The shallow minimum in the OR slope at $w/n = 2L/3$ is captured by both numerical simulations and theory.

To connect the voltage shift (4) to actual voltage signals for different bulk target concentrations C or charge concentration in Figures 2 and 3, we extend the above theories from two-dimensions to three dimensions and assume adsorption equilibrium. This involves correcting for the unblocked membrane area $\chi = 1 - \left(\frac{n}{w}\right)^2(d + 2\lambda_0)^2\pi$ and the shear force for the symmetry-breaking vortex transition, $V_o = \left(\frac{2nl}{w}\right)^2 \left(\frac{RT}{zF}\right)$. We can relate the particle surface density to the bulk concentration by the dissociation constant of the adsorption equilibrium, $\left(\frac{w}{nl_s}\right)^2 = \frac{1}{\theta} = \frac{K_D}{C}$ or $\left(\frac{n}{w}\right)^2 = \frac{C}{l_s^2 K_D}$ where l_s is the site, probe, or charge spacing, θ is the sites occupied, and K_D is the dissociation constant with units of M. For nanoparticles, the probe spacing is just the maximum packing distance of $l_s = d$. Hence, $V_o = \left(\frac{C}{K_D}\right) \left(\frac{2l}{l_s}\right)^2 \left(\frac{RT}{zF}\right)$ and the minimum slope occurs at $C_{\min} = K_D \left(\frac{3l_s}{2L}\right)^2$. Hence, knowing the concentration where the minimum slope occurs and knowing the diffusion length in the UR region L , one can determine the important parameter $l_s^2 K_D$. Once that is known, $V_o = \left(\frac{2l}{l_s}\right)^2 \left(\frac{C}{K_D}\right) \left(\frac{RT}{zF}\right) = \left(\frac{3l}{L}\right)^2 \left(\frac{C}{C_{\min}}\right) \left(\frac{RT}{zF}\right)$ can also be expressed as a function of C or the concentration at the minimum slope. Hence, the voltage shift we have defined to quantify C can be expressed as

$$\Delta V \sim (V_o(C) - V_o(0)) = \left(\frac{C}{C_{\min}} \right) \left(\frac{3l}{L} \right)^2 \left(\frac{RT}{zF} \right) \quad (7)$$

This relationship between C and the voltage shift quantitatively captures our measured voltage shift data below $C_{\min} \sim 40 \mu\text{M}$, as shown in the Figure 2e. The minimum occurs because the increasing vortex size (with decreasing C) produces a vortex that reaches the natural diffusion length L , which is found to be roughly 2.5 μm for this experiment. This thin diffusion layer suggests the presence of a convective boundary layer, which is consistent with the observation of a strong vortex flow in that report.¹⁶ Using this value of L and $l =$

8 μm , we plotted the theoretical prediction (6) for the slope in the OR region, with the new χ for a planar membrane surface, in Figure 2d. Like the voltage shift, the theory captures the slope below C_{\min} but breaks down near C_{\min} . We suspect this breakdown of the theory near C_{\min} to be because of the onset of water splitting at high concentrations,¹⁶ which is not captured in the current theory. The highly concentrated negative charge nucleic acid layer on top of the oppositely charged membrane has been suggested to form a bipolar layer capable of splitting water.¹⁷

The final piece of the puzzle is when w/n is much larger than l , the natural vortex length of 8 μm , when equal spacing of the particles cannot be guaranteed. (For dense packing, electrostatic repulsion between the probes would favor a more periodic spacing.) The vortices then take on this natural length scale l without any influence from the nanoparticles or macromolecules. The charged particles and molecules hence produce a mean field that opposes the applied field. They simply increase V_o , the voltage required to pull out an extended polarized layer, and the critical electric force necessary to affect the symmetry-breaking vortex transition by a finite value. We estimate this voltage shift by the effective ζ potential introduced by these surface particles/molecules. Since the surface concentration of surface charge is $C_s = (z_s C / K_D l_s^2)$, where z_s is the charge per molecule or reporter, one can integrate the nonlinear Poisson–Boltzmann equation to look at the resulting voltage drop across the EPL due to the presence of these charges.⁵ This is essentially the Guoy–Chapman theory and for large potential drop ($>RT/F$), the effect of the surface charge produces a voltage shift of

$$\Delta V = \left(\frac{2RT}{zF} \right) \ln \left(\frac{z_s C_s}{c_0 \lambda_0} \right) \\ = \left(\frac{RT}{zF} \right) (2 \ln 10) \log_{10} \left(\frac{z_s C}{c_0 \lambda_0 K_D l_s^2} \right) \quad (8)$$

where c_0 is the ionic strength in the bulk and the Debye length is evaluated at the DI condition in the depletion region. This equation predicts that for every decade change in concentration C , we obtain $2 \ln 10 (RT/F)$ or about 0.12 V voltage shift in a unit-valent electrolyte ($z = 1$), provided there is a charge on the target molecule or reporter ($z_s \neq 0$). This is consistent with the low concentration calibration curves we have measured for nanoparticles, DNA and RNA in Figure 3, which shows shift per decade of 0.14 to 0.19 V for nucleic acids, endotoxins, and proteins in nanoparticle reporters, close to the theoretical value of 0.12 V per decade. The additional shift most likely arises from voltage thresholds for ion entry into the membrane and charge transfer at the electrodes, which would be system dependent. The shifts in Figure 3 that determine the magnitude ΔV of the signal are hence due to different dissociation constants, probe densities, charge per target molecule and different ionic strengths of the bulk buffer c_0 . It is expected that the limit of detection occurs when ΔV is less than the thermal noise (RT/F), or when the quantity in the parentheses is of unit order. Hence, universal standard curve (8) suggests that this limit of detection is inversely proportional to the number of charges z_s per reporter and one can quantify at lower C values by using reporters with more charge, even for membranes with small probe density (high l_s) and low target affinity (high K_D). More specifically, the key parameter $\frac{z_s}{c_0^2 \lambda_0 l_s^2}$ can be decomposed into $(\pi \sigma_s / c_0 \lambda_0)$ where σ_s is

the surface density of charges on the reporter and the maximum packing distance l_s is taken to be the reporter diameter d . If the depletion action extends into the bulk, such that $c_0 = 10^{-7} \text{ M}$ (DI conditions) near the membrane surface (see Figure 6) and the DI Debye length of $\lambda_0 = 100 \text{ nm}$, the quantity $\sigma_s \lambda_0$ is roughly $1.0 \mu\text{m}^{-2}$. Considering that the surface density σ_s of charges on the silica nanoparticle is about 1000 per μm^2 , the nanoparticle can hence increase the detection limit below K_D by a factor of 1000. This sensitivity enhancement by charged nanoparticle reporters is evident in the protein data of endothelin-1 of Figure 3, with subpicomolar sensitivity for a sandwich assay with typical $K_D \sim \text{nM}$ dissociation constants. The membrane size or diffusion length L does not enter into the voltage shift of (8). Consequently, the voltage signal is independent of the sensor dimension or material, as long that the membrane is sufficiently ion-selective. The universal voltage shift expression (8) can be used as a standard calibration curve for all membrane sensors.

CONCLUSIONS

Charged molecules or nanoparticles on the surface of a perm-selective membrane are shown to shift the transition voltage V_o between LR and OR of the I – V curve. No other part of the I – V curve is significantly affected by the presence of the molecules at low target concentrations ($w/n \gg 1$). This is hence a built-in control to determine if the sensor is operating properly after target hybridization—the UR and LR region should be unaffected by the surface molecules.

That the OR region involves ion depletion and microvortices suggests that the sensor is robust to bulk ionic strength and nonspecific binding, particularly protein fouling of the hydrophilic charged membrane surface. Blocking of the sensor surface was never necessary. Indeed, the derived universal standard curve has a voltage that only has a weak $\ln c_0$ dependence on the bulk ion concentration. The depletion action also reduces the screening of charged targets and charged nanoparticle reporters, to produce sensitivity enhancement. The nanoparticle reporter, with its larger hydrodynamic radius than the antigen, can enhance wash-induced selectivity. That the size of the charge target molecules/reporters and the sensor area are also irrelevant suggest the universal calibration curve is valid for all targets and all membrane sensors. These universality features arise from the scale-invariant ion transport phenomena that governs the I – V curve, including an asymmetric vortex bifurcation that reduces the size of the dominant vortex by half and hence decreases the differential resistance by a factor of 2. The transition voltage V_o is due a threshold electrokinetic force requires to drive the vortex bifurcation. Since this threshold force is independent of the universal ion transport dynamics, it is the only part of the I – V curve that is dependent on the target concentration C . It occurs at a particular (current) and involves a large voltage shift ($\gg RT/F$) that has a $\ln C$ dependence to produce a sensitive and yet large dynamic range sensor signal. It is a rather unique and novel biosensor mechanism that has many advantages, including sensitivity, selectivity, large dynamic range, and robustness to sensor dimension and chemical structure of the charged targets.

AUTHOR INFORMATION

Corresponding Author

Hsueh-Chia Chang – Department of Aerospace and Mechanical Engineering, University of Notre Dame, Notre

Dame, Indiana 46556, United States; Department of Chemical and Biomolecular Engineering, University of Notre Dame, Notre Dame, Indiana 46556, United States; Phone: 1-574-631-5697; Email: hchang@nd.edu

Authors

- Sebastian Sensale – Department of Aerospace and Mechanical Engineering, University of Notre Dame, Notre Dame, Indiana 46556, United States;  orcid.org/0000-0003-0502-5138
- Zeinab Ramshani – Department of Chemical and Biomolecular Engineering, University of Notre Dame, Notre Dame, Indiana 46556, United States
- Satyajyoti Senapati – Department of Chemical and Biomolecular Engineering, University of Notre Dame, Notre Dame, Indiana 46556, United States

Complete contact information is available at:
<https://pubs.acs.org/10.1021/acs.jpcb.0c09916>

Author Contributions

S. Sensale performed the numerical simulations, developed the theory, and wrote the manuscript. Z. Ramshani and S. Senapati designed the sensors and performed the experiments. H.-C. Chang developed the theory and directed the research. All authors contributed to the writing.

Notes

The authors declare no competing financial interest.

ACKNOWLEDGMENTS

Research was sponsored by the Office of the Secretary of Defense and was accomplished under Agreement Number W911NF-17-3-003. The views and conclusions contained in this document are those of the authors and should not be interpreted as representing the official policies, either expressed or implied, of the Office of the Secretary of Defense or the U.S. government. This work was also partially supported by the NIH Commons Fund, through the Office of Strategic Coordination/Office of the NIH Director, 1UG3CA241684-01.

REFERENCES

- (1) Berzina, B.; Anand, R. Tutorial Review: Enrichment and Separation of Neutral and Charged Species by Ion Concentration Polarization Focusing. *Anal. Chim. Acta* **2020**, *1128*, 149.
- (2) Slouka, Z.; Senapati, S.; Chang, H.-C. Microfluidic Systems with Ion-Selective Membranes. *Annu. Rev. Anal. Chem.* **2014**, *7* (1), 317–335.
- (3) Chang, H.-C.; Yossifon, G.; Demekhin, E. A. Nanoscale Electrokinetics and Microvortices: How Microhydrodynamics Affects Nanofluidic Ion Flux. *Annu. Rev. Fluid Mech.* **2012**, *44* (1), 401–426.
- (4) Levich, V. G. *Physicochemical Hydrodynamics*; Prentice-Hall: 1962.
- (5) Chang, H.; Yeo, L. *Electrokinetically Driven Microfluidics and Nanofluidics*; Cambridge University Press: 2010.
- (6) Rubinstein, I.; Shtilman, L. Voltage against Current Curves of Cation Exchange Membranes. *J. Chem. Soc., Faraday Trans. 2* **1979**, *75* (0), 231–246.
- (7) Ben, Y.; Chang, H.-C. Nonlinear Smoluchowski Slip Velocity and Micro-Vortex Generation. *J. Fluid Mech.* **2002**, *461*, 229–238.
- (8) Yossifon, G.; Mushenheim, P.; Chang, Y.-C.; Chang, H.-C. Nonlinear Current-Voltage Characteristics of Nanochannels. *Phys. Rev. E* **2009**, *79* (4), 046305.
- (9) Mani, A.; Wang, K. M. Electroconvection Near Electrochemical Interfaces: Experiments, Modeling, and Computation. *Annu. Rev. Fluid Mech.* **2020**, *52* (1), 509–529.
- (10) Rubinstein, I.; Zaltzman, B. Electro-Osmotically Induced Convection at a Permselective Membrane. *Phys. Rev. E: Stat. Phys., Plasmas, Fluids, Relat. Interdiscip. Top.* **2000**, *62* (2), 2238–2251.
- (11) Rubinstein, S. M.; Manukyan, G.; Staicu, A.; Rubinstein, I.; Zaltzman, B.; Lammertink, R. G. H.; Muggele, F.; Wessling, M. Direct Observation of a Nonequilibrium Electro-Osmotic Instability. *Phys. Rev. Lett.* **2008**, *101* (23), 236101.
- (12) Yossifon, G.; Chang, H.-C. Selection of Nonequilibrium Overlimiting Currents: Universal Depletion Layer Formation Dynamics and Vortex Instability. *Phys. Rev. Lett.* **2008**, *101* (25), 254501.
- (13) Senapati, S.; Slouka, Z.; Shah, S. S.; Behura, S. K.; Shi, Z.; Stack, M. S.; Severson, D. W.; Chang, H.-C. An Ion-Exchange Nanomembrane Sensor for Detection of Nucleic Acids Using a Surface Charge Inversion Phenomenon. *Biosens. Bioelectron.* **2014**, *60*, 92–100.
- (14) Ramshani, Z.; Zhang, C.; Richards, K.; Chen, L.; Xu, G.; Stiles, B. L.; Hill, R.; Senapati, S.; Go, D. B.; Chang, H.-C. Extracellular Vesicle MicroRNA Quantification from Plasma Using an Integrated Microfluidic Device. *Communications Biology* **2019**, *2* (1), 1–9.
- (15) Slouka, Z.; Senapati, S.; Shah, S.; Lawler, R.; Shi, Z.; Stack, M. S.; Chang, H.-C. Integrated, DC Voltage-Driven Nucleic Acid Diagnostic Platform for Real Sample Analysis: Detection of Oral Cancer. *Talanta* **2015**, *145*, 35–42.
- (16) Taller, D.; Richards, K.; Slouka, Z.; Senapati, S.; Hill, R.; Go, D. B.; Chang, H.-C. On-Chip Surface Acoustic Wave Lysis and Ion-Exchange Nanomembrane Detection of Exosomal RNA for Pancreatic Cancer Study and Diagnosis. *Lab Chip* **2015**, *15* (7), 1656–1666.
- (17) Slouka, Z.; Senapati, S.; Yan, Y.; Chang, H.-C. Charge Inversion, Water Splitting, and Vortex Suppression Due to DNA Sorption on Ion-Selective Membranes and Their Ion-Current Signatures. *Langmuir* **2013**, *29* (26), 8275–8283.
- (18) Senapati, S.; Basuray, S.; Slouka, Z.; Cheng, L.-J.; Chang, H.-C. A Nanomembrane-Based Nucleic Acid Sensing Platform for Portable Diagnostics. *Top. Curr. Chem.* **2011**, *304*, 153–169.
- (19) Yin, Z.; Ramshani, Z.; Waggoner, J. J.; Pinsky, B. A.; Senapati, S.; Chang, H.-C. A Non-Optical Multiplexed PCR Diagnostic Platform for Serotype-Specific Detection of Dengue Virus. *Sens. Actuators, B* **2020**, *310*, 127854.
- (20) de Valençā, J.; Jōgi, M.; Wagterveld, R. M.; Karatay, E.; Wood, J. A.; Lammertink, R. G. H. Confined Electroconvective Vortices at Structured Ion Exchange Membranes. *Langmuir* **2018**, *34* (7), 2455–2463.
- (21) Davidson, S. M.; Wessling, M.; Mani, A. On the Dynamical Regimes of Pattern-Accelerated Electroconvection. *Sci. Rep.* **2016**, *6* (1), 22505.
- (22) Bellón, T.; Polezhaev, P.; Vobecká, L.; Slouka, Z. Fouling of a Heterogeneous Anion-Exchange Membrane and Single Anion-Exchange Resin Particle by SsDNA Manifests Differently. *J. Membr. Sci.* **2019**, *572*, 619–631.
- (23) Chang, H.-C.; Demekhin, E. A.; Shelistov, V. S. Competition between Dukhin's and Rubinstein's Electrokinetic Modes. *Phys. Rev. E* **2012**, *86* (4), 046319.
- (24) Roberts, R. M.; Chang, H.-C. Wave-Enhanced Interfacial Transfer. *Chem. Eng. Sci.* **2000**, *55* (6), 1127–1141.